Plane-Wave Ultrasound Beamforming Through Independent Component Analysis

Sobhan Goudarzi*, Amir Asif, and Hassan Rivaz

Department of Electrical and Computer Engineering, Concordia University, Montreal, QC, Canada.

Abstract

Background and Objective: Beamforming in coherent plane-wave compounding (CPWC) is an essential step in maintaining high resolution, contrast and framerate. Adaptive methods have been designed to achieve this goal by estimating the apodization weights from echo traces acquired by several transducer elements.

Methods: Herein, we formulate plane-wave beamforming as a blind source separation problem, where the output of each transducer element is considered as a non-independent observation of the field. As such, beamforming can be formulated as the estimation of an independent component out of the observations. We then adapt the independent component analysis (ICA) algorithm to solve this problem and reconstruct the final image.

Results: The proposed method is evaluated on a set of simulations, real phantom, and *in vivo* data available from the plane-wave imaging challenge in medical ultrasound. Moreover, the results are compared with other well-known adaptive methods.

Conclusions: Results demonstrate that the proposed method simultaneously improves the resolution and contrast.

Keywords: Plane-wave imaging, adaptive beamforming, ICA, image quality.

*Corresponding author
Email address: sobhan.goudarzi@concordia.ca (Sobhan Goudarzi)

1. Introduction

Ultrasound imaging experienced a revolution with the introduction of plane-wave imaging (PWI) in which frame-rate can reach several thousands per second. In contrast to other techniques, PWI fires all elements of the probe simultaneously to form a flat wavefront and span the whole region of interest in a single shot. This technique has been successfully applied to different applications such as imaging of shear waves, contrast imaging, and Doppler imaging of blood flow [1]. Having an unfocused transmitted beam, however, leads to poor resolution and low contrast in PWI. This drawback was addressed by coherent compounding of images obtained by several insonifications of different angles [2]. Consequently, there is always a trade-off between image quality and frame-rate. Hence, beamforming is witnessing a growing attention in order to enhance the quality of images without sacrificing the frame-rate.

In PWI, beamforming mainly refers to the method of merging the outputs of different crystal elements. More specifically, it applies a weighting function across the receive aperture which is referred to as apodization. It can also be used during transmission. Delay-and-sum (DAS) is a classical nonadaptive beamforming method in which apodization weights for different pixels of the image are assigned based on the F-number (f#) as well as a predefined window shape. As known from spectral estimation, there is often a trade-off between the width of main lobe and energy of side lobes of the apodization window. When measured backscattered signals are directly used to optimize the apodization weights, the beamforming method is considered adaptive.

Capon or minimum variance (MV) is a well-known adaptive method in which apodization weights are estimated to minimize the variance of output while preserving the unity gain in the steering direction [3]. Asl and Mahloojifar [4] proposed another implementation of the MV, referred to as eigenspace-based MV (EMV) based on eigenspace and eigenvectors for suppressing off-axis signals. The main issue with MV is that we cannot estimate the data covariance matrix accurately. In addition, estimation of the covariance matrix of data is time

consuming and makes it impractical for real-time applications [5, 6].

A family of adaptive beamforming algorithms is based on phase coherence. First, the coherence factor (CF) is defined as the ratio between the coherent and incoherent energy across the aperture [7] and then used as an adaptive weight following the DAS beamformer to enhance the image quality [8]. CF was generalized to be computed from Fourier spectra over the aperture of the delayed channel data and in a range of low spatial frequency region [8]. Subsequently, Camacho *et al.* [9] used phase information of aperture data to compute the adaptive correction weight and proposed phased CF (PCF). However, the estimated correction weights of CF methods can be affected by speckle noise.

More recently and specifically for PWI, the MV approach was applied in [10, 11, 12, 13]. Nguyen and Prager [14] proposed extensions to MV for coherent plane-wave compounding (CPWC). Beamforming based on compressive sensing for PWI was introduced in [15, 16, 17, 18]. Dei *et al.* [19, 20] investigated the performance of their beamforming method entitled aperture domain model image reconstruction (ADMIRE) on PWI. Beamforming in Fourier domain on PWI was first proposed by Lu [21], and then applied with two distinct strategies by Garcia *et al.* [22] and Bernard *et al.* [23]. Beamforming as a regularized inverse problem was introduced in [24] and applied at different depths separately. This point of view was extended in [25] to solve inverse problem for all image depths jointly. Recently, a statistical interpretation of beamforming entitled iterative maximum-a-posteriori (iMAP) was introduced in [26].

Herein, we propose a new framework for adaptive plane-wave beamforming wherein apodization weights are estimated through independent component analysis (ICA). In the field of US imaging, ICA has been mainly used for clutter filtering and noise suppression [27, 28, 29, 30, 31, 32]. Recently, ICA was used as a dimensionality reduction technique to speed up ADMIRE beamforming [33].

An overview of the proposed method is shown in Fig. 1. When an ultrasound wave is transmitted into the field, the most popular way to trace back the backscattered wave corresponding to each pixel of the target is by applying the associated propagation delay to each signal recorded by piezoelectric elements

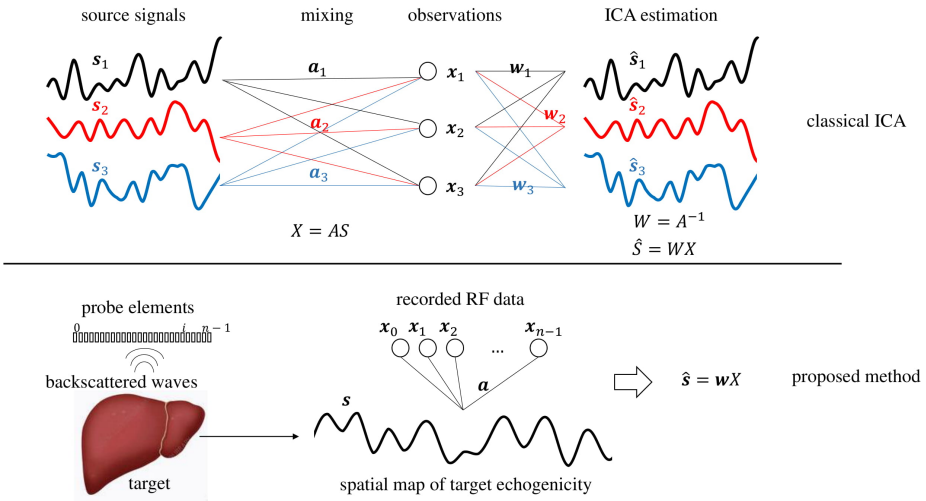

Figure 1: An overview of the proposed method and its correspondence with classical ICA. In the top, three sources are reconstructed using three observations. In the bottom, the source is 2D spatial echogenicity map, and the vectorized source s is reconstructed using n observations.

of the probe. Consequently, a discrete spatial map of the target echogenicity can be constructed as an ultrasound image. However, there is also the possibility of source ambiguity. More specifically, the backscattered waves from pixels at equal distances from the piezoelectric element lead to a single sensory data at the resulting RF signal. This physical limitation brought about by wave propagation is what motivates us to make use of ICA to suppress the pixel correlation in the imaging field after spatiotemporal mapping. Fortunately, the group of pixels which are indistinguishable from the output of each piezoelectric element are not the same. Therefore, our approach considers the signal recorded by each piezoelectric element as a non-independent observation of the target echogenicity and then uses ICA, as an adaptive beamforming method, to extract the independent spatial map of target echogenicity. Herein, the independency of spatial map means that each sample contains the trace of only one pixel. In the proposed method, the apodization window is first estimated using ICA algorithm, and then it is applied throughout the image based on a predefined f-number (f#). The performance of the proposed adaptive plane-wave beam-

forming is evaluated and compared to other methods on a set of simulation, phantom, and *in vivo* data provided by PWI challenge in medical ultrasound (PICMUS) 2016 [34].

2. Methods

Consider a linear array of n crystal elements, symmetrically distributed on the x-axis, transmitting along the positive z-axis (Fig. 2(a)). Let us assume that a plane-wave with angle α spans the domain with a sound speed of c. The backscattered signals received by crystal element i located at x_i is denoted by $\mathbf{h}_i(t)$ (Fig. 2(b)). Without any loss of generality, $zcos(\alpha) + xsin(\alpha)$ is the transmission distance d_t from the origin of the transmitted plane-wave to an arbitrary point (x, z) in the region-of-interest (ROI) and $\sqrt{(x - x_i)^2 + z^2}$ is the receiving distance d_r from (x, z) to the location of crystal element i (for more details see [2]). Let us define R_i as a matrix containing the RF data recorded by crystal element i corresponding to each point (x, z) in the ROI and its elements can be found by applying the associated propagation delay to $\mathbf{h}_i(t)$ as follows (hereafter, capital and bold font variables represent matrices and vectors, respectively):

$$\tau(x, z) = \frac{d_t + d_r}{c} \Longrightarrow R_i(x, z) = \mathbf{h}_i(\tau(x, z)), \tag{1}$$

As shown in Eq. (1), each piezoelectric element gives one RF matrix of the ROI (vectorized R_i are denoted by $\mathbf{r}_i$ and shown in Fig. 2(c)). Therefore, the beamformed RF matrix S (Fig. 2(f)) is the result of information fusion among different crystal elements, and each element of $S(x, z)$ can be obtained through the following weighted summation:

$$S(x, z) = \sum_{i=0}^{n-1} \mathbf{w}_i(x, z) R_i(x, z), \tag{2}$$

where $\mathbf{w}$ is the apodization window of length n (Fig. 2(e)). In practice, however, we utilize dynamic beamforming where the f# is fixed for the entire image.

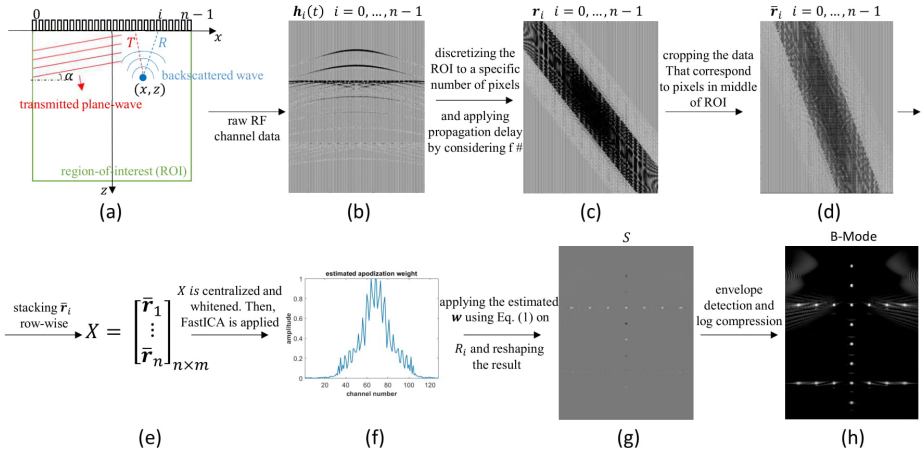

Figure 2: The proposed adaptive beamforming pipeline. (a) Geometrical illustration of the PWI. (b) The plot of backscattered signals recorded by piezoelectric elements. (c) The plot of vectorized RF matrices constructed by applying propagation delay to raw RF channel data by considering the f#. (d) The plot of vectorized cropped RF matrices corresponding to pixels in the middle of ROI. (e) The observation matrix of ICA constructed by stacking $\bar{\mathbf{r}}_i$ row-wise. (f) The estimated apodization window using ICA. (g) The beamformed RF matrix S. (h) The final B-Mode image.

Therefore, l is defined as the number of crystal elements considered for the reconstruction of each depth (z) of the image and is calculated as follows [2]:

$$f\# = z/l. \tag{3}$$

After construction of S, it is subject to envelope detection and *log* compression in order to obtain the final B-Mode ultrasound image (Fig. 2(g)). Herein, our goal is to estimate the apodization window $\mathbf{w}$ using ICA.

2.1. Independent Component Analysis

A full mathematical description of ICA is provided in [35]. We include a short summary here to make this paper self-contained. Our proposed method is explained in the next section. ICA is a framework used to separate signal components mixed in observations recorded at different transducer elements [35]. Assuming an n-dimensional signal space, i.e., an n-dimensional observed data

$\mathbf{x}$, n-dimensional independent sources $\mathbf{s}$, and a square transformation matrix W of size $n \times n$, the mixing model can be written as follows [35]:

$$\mathbf{s} = W\mathbf{x}. \tag{4}$$

With the assumption of having independent and non-Gaussian sources (at the most one independent Gaussian source is allowed), both W and $\mathbf{s}$ can be estimated using the ICA algorithm. In practice, the objective function for ICA estimation can be formulated using different measures of non-Gaussianity such as kurtosis, negentropy, and mutual information. Moreover, it is very useful to center and whiten the observations before applying ICA. One of the most famous algorithms of ICA implementation is FastICA, where a unit vector $\mathbf{w}$ is computed such that the dot product $\mathbf{w}^T\mathbf{x}$ maximizes negentropy. The FastICA algorithm can be summerized in four steps as follows [35]:

1. Random initialization of vector $\mathbf{w}$.
2. $\mathbf{w}_{new} = E\{\mathbf{x}g(\mathbf{w}^T\mathbf{x})\} - E\{g'(\mathbf{w}^T\mathbf{x})\}\mathbf{w}$
3. $\mathbf{w} = \mathbf{w}_{new}/\|\mathbf{w}_{new}\|$
4. Return to step 2 until the direction of $\mathbf{w}$ does not change.

notation E refers to the expectation operation. Symbols g and g' are first and second derivatives of a non-quadratic nonlinear function f, respectively. It was shown that either of the two functions f is robust for negentropy estimation [36]:

$$f(u) = \frac{1}{a_1}\log\cosh(a_1 u), \text{ or } f(u) = -\exp(-u^2/2). \tag{5}$$

where $1 \leq a_1 \leq 2$.

More details regarding the FastICA algorithm can be found in [35].

2.2. Beamforming Using ICA

In general, our goal is to reconstruct a high-quality ultrasound image which is a spatial map of the target echogenicity. More specifically, we discretize the map of scatterers that leads to pixels. Each pixel corresponds to an averaged tissue reflectivity function over the extent of the pixel. When the RF data

corresponding to each pixel of the final image is extracted from the output of each crystal element (using Eq. (1)), there is also the possibility of source ambiguity. More specifically, the backscattered waves of at least two different pixels at equal distances from the piezoelectric element arrive simultaneously and lead to a single sensory data at the resulting RF signal. In this section, first, this problem is mathematically demonstrated and then our proposed solution is explained.

Without loss of generality, when $\alpha = 0$, the backscattered waves of two distinct pixels (with indices 1 and 2) arrive at the same time in crystal element i if and only if they have the same propagation delay τ. Form Eq. (1) and if the first pixel is in the lateral position x_i, it can be written that:

$$\tau_1 = \tau_2 \Longrightarrow 2z_1 = z_2 + \sqrt{(x_2 - x_i)^2 + z_2^2}. \tag{6}$$

Moving z_2 to the left side of the equality and squaring both sides, we get:

$$4z_1^2 + z_2^2 - 4z_1 z_2 = (x_2 - x_i)^2 + z_2^2. \tag{7}$$

Cancelling z_2^2 from both sides, the resulting expression can be rearranged as:

$$4z_1 z_2 = 4z_1^2 - (x_2 - x_i)^2. \tag{8}$$

Diving both sides by $4z_1$ (which is always nonzero) gives:

$$z_2 = z_1 - \frac{(x_2 - x_i)^2}{4z_1}. \tag{9}$$

So, for $z_2 < z_1$, there are a bunch of pixels located on an ellipse, whose reflections arrive at the same time as for pixel 1. In other words, all those pixels have the same value in the extracted RF matrix $R_i(x, z)$ from Eq. (1). In the continuous case, this problem is fully addressable. In the discrete case, however, there is the error due to quantization as well. Although this problem was shown for the specific case of $\alpha = 0$, the concept can be extended for different angles.

As seen from Eq. (9), the group of scatterers from whom reflections arrive simultaneously are not the same for each crystal element. In other words, the

group of indistinguishable pixels in each $R_i(x, z)$ is distinct. This point provides the opportunity of source separation using ICA. If we consider each $\mathbf{r}_i$ as a non-independent observation of the discretized map of scatterers, our task is to extract the beamformed RF matrix S out of these non-independent observations (Eq. (2)). Therefore, we adapt ICA to estimate the apodization window $\mathbf{w}$. In the ideal case, the explained pixel correlation in the imaging field after spatiotemporal mapping is perfectly suppressed, and the desired S contains independent elements containing the trace of only one distinct pixel. It has to be mentioned that in practice, the axial and lateral resolutions are based on the sampling frequency of the system, center frequency of the transmitted wave, and transducer design. So, one pixel results in one voxel of the ROI.

In ultrasound beamforming, an issue is that the apodization window is not fixed throughout the image. More specifically, ICA works with a fixed transformation matrix W in Eq. (4). In ultrasound images, however, the apodization weight is not spatially invariant, rendering a different set of weights for different pixels. Two points make the apodization weights spatially variant. First, for pixels lying at the two lateral ends of the image, there are crystal elements predominately lying along one side. Second, as explained in Section 2, pixels at different depths of the image are reconstructed using a different number of elements to keep the f# fixed across the entire image. Hence, if we do not consider these points, ICA fails to estimate the source and apodization windows, leading to images that are even lower in quality than DAS.

To solve the aforementioned problem, first, we consider the f# while constructing the $R_i(x, z)$ (Fig. 2(c)). More specifically, $R_i(x, z)$ contains a nonzero value only if crystal element i is considered for reconstructing depth z of the image (Eq. (3)). Second, we consider only the central pixels of the image around which the crystals are symmetric as the input to the ICA algorithm (Fig. 2(d)). In this way, the cropped portion of $\mathbf{r}_i$ is used to construct the observation matrix X. In our ICA formulation, therefore, the observations are RF data corresponding to central pixels of final image that are recorded by crystal elements of the probe. It has to be mentioned that the random initialization of the transforma-

tion matrix W only affects the number of iterations that the algorithm takes to converge, and it does not lead to any variation in the results after beamforming.

As shown in Fig. 2, our proposed adaptive beamforming algorithm for PWI using ICA includes the following steps:

1. The region of interest is discretized into pixels. By considering a specific f#, the propagation delays are applied to the raw RF channel data to generate $\mathbf{r}_i, i = 0, ..., n-1$ (Fig. 2(c)).
2. Each $\mathbf{r}_i$ is considered as an observation of the field. First, it is cropped (denoted by $\bar{\mathbf{r}_i}$) and then the observation matrix X is constructed by stacking the row vectors ($\bar{\mathbf{r}_i}$). Finally, matrix X is centralized and whitened before running ICA (Fig. 2(d-e)).
3. The independent source and corresponding mixing vector are estimated using the FastICA algorithm [37] by maximizing Negentropy as the measure of non-Gaussianity (Fig. 2(f)).
4. The apodization window (the estimated transformation vector in the last step) is applied throughout the image based on a predefined f# (Fig. 2(g)).

In step 3, apodization window $\mathbf{w}$ is iteratively updated to maximize negentropy (estimated using $f(u) = -\exp(-u^2/2)$) with respect to $\mathbf{w}^T X$. More specifically, the fixed-point iteration scheme [37] uses g and g' which are first and second derivatives of the non-quadratic nonlinear function f to find the optimal value of $\mathbf{w}$. As discussed in [35], the number of sources, in the ICA algorithm, has to be equal or less than the number of observations. ICA can be considered as a variant of the projection pursuit algorithm [38], which enables one-by-one estimation of the independent components. Herein, the number of independent sources in the ICA algorithm is set to one since we only look for a single source, which is a collection of all scatterers. This is an important feature that substantially reduces the computational load.

2.3. Experiments

2.3.1. Dataset

In this section, we use a publicly available PWI dataset, entitled PICMUS, which was provided by the IEEE International Ultrasonics Symposiun (IUS 2016) in order to benchmark novel beamforming methods [34]. The PICMUS data utilized in this work include:

1. Simulation resolution (SR): A simulated ultrasound image containing point targets distributed vertically and horizontally over an anechoic background designed to assess the performance of beamforming methods in terms of spatial resolution.
2. Simulation contrast (SC): A simulated ultrasound image containing anechoic cysts distributed vertically and horizontally over fully developed speckle designed to assess the performance of beamforming methods in terms of contrast.
3. Experimental Resolution (ER): An experimental ultrasound image was recorded on a CIRS Multi-Purpose Ultrasound Phantom (Model 040GSE) in the regions containing several wires against speckle background to assess the performance of beamforming methods in terms of spatial resolution.
4. Experimental contrast (EC): An experimental ultrasound image was recorded on the same phantom as ER but in the regions containing two anechoic cysts against speckle background to assess the performance of beamforming methods in terms of contrast.

In addition, PICMUS dataset also contains two *in vivo* ultrasound images, showing cross-sectional and longitudinal views, recorded on the carotid artery of a volunteer. All of the phantom and *in vivo* data were collected using a Verasonics Vantage 256 research scanner and a L11 probe (Verasonics Inc., Redmond, WA). The simulation settings were selected to be as similar as possible to the experimental setup.

For each of mentioned groups, a collection of received prebeamformed data corresponding to 75 steered Plane-Waves covering the angle span from -16° to

16° was provided. Both RF and IQ (phase quadrature) formats of data were provided. The proposed algorithm works on the RF version of data. More details regarding PICMUS dataset can be found in [34].

2.3.2. Evaluation Metrics

Contrast and resolution are considered for the sake of evaluation. More specifically, resolution is estimated as the full width at half maximum (FWHM) both in axial and lateral directions. The average value of FWHM among all scatterers in the image is reported. As for contrast, the contrast to noise ratio (CNR) is calculated as follows [34]:

$$\mathrm{CNR} = 20\log_{10}\left(\frac{\mid \mu_{in} - \mu_{out} \mid}{\sqrt{(\sigma_{in}^2 + \sigma_{out}^2)/2}}\right), \tag{10}$$

where μ and σ are the mean gray level and the gray level standard deviation. Subscribes $._{in}$ and $._{out}$ refer to inside and outside of the anechoic cystic region, respectively. Indexes are calculated on B-Mode images. In order to unify the comparison, we use the codes provided by PICMUS to compute the indexes.

2.3.3. Implementation Details

As explained in Section 2.2, the FastICA algorithm is used to estimate the apodization window. The maximum number of iterations is set to 100 and the stopping criterion is set to be $\epsilon = 10^{-6}$. The weights are initialized with random numbers extracted from standard distribution. The reduction of dimension through PCA is not used and the best results which are most reproducible are attained by considering all eigenvalues in the estimation procedure. We use the Matlab implementation of the Fixed point ICA, the main algorithm of FastICA, which is publicly available online `http://research.ics.aalto.fi/ica/fastica/code/dlcode.shtml`.

Throughout the results section, we consider $f\# = 1.75$ and use Tukey (tapered cosine) window with constant parameter set to 0.25 for DAS and other adaptive methods on top of DAS.

It is not possible to theoretically prove the convergence of FastICA algorithm with the mentioned parameters. In practice, however, we set the maximum

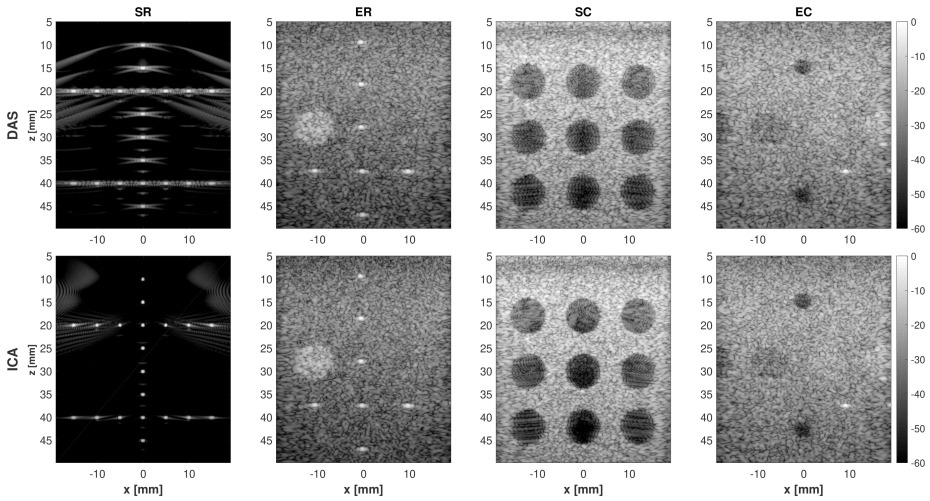

Figure 3: Beamforming results on the single 0° plane wave. Columns indicate different image data sets while rows correspond to beamforming methods.

number of iterations equal to 100 and observe that for all of data sets, the algorithm converges in a lower number of iterations.

3. Results

3.1. Simulated and Experimental Data

The results of DAS beamforming versus our proposed method based on ICA on a single 0° plane wave of simulated and experimental data are illustrated in Fig. 3. As seen from this figure, the proposed beamforming method outperforms DAS and improves the resolution as well as contrast on both simulated and experimental phantom data. In order to better investigate the amount of improvement, the quantitative indices are reported in Table 1. What causes the improvement is the window used for apodization. So, as Table 1 confirms, improvement in resolution can only be acquired in the lateral direction. The highest improvement in lateral FWHM is 36.5% on simulated plane-wave data of only one single transmission. In terms of CNR, approximately 9% of improvement is achieved on the experimental cyst data of a single transmission while boarders of the cyst are also sharper. As mentioned before, for pixels lying at

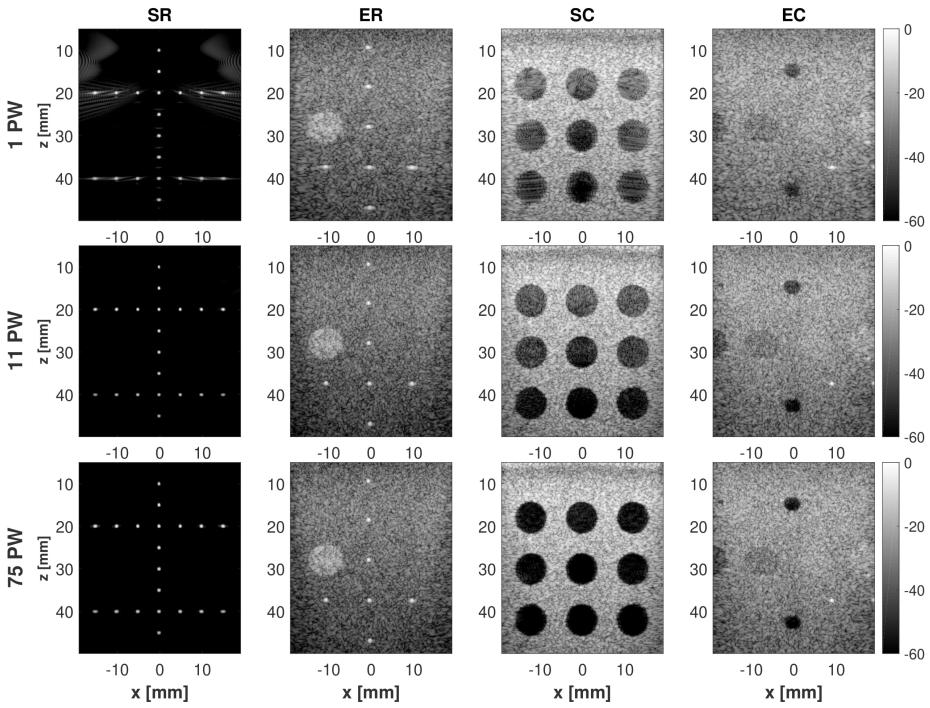

Figure 4: ICA beamforming using 1, 11, and 75 plane waves. Columns indicate different image data sets and rows correspond to the number of transmitted plane waves.

the two lateral ends of the image, symmetrical channel data is not available and data is predominately limited to one side. This point forced us to only consider the central pixels of the image. Therefore, there will be a reduction in image quality in those border regions because the weights are not optimized for those region. Furthermore, this reduction in quality is more visible in shallow regions of the image (the reconstructed SR image with ICA in Fig. 3) since a limited number of elements are considered for the reconstruction of pixel intensities. It has to be mentioned that this problem is one of limitations of ultrasound imaging regardless of the beamforming method.

In order to investigate the effect of CPWC, the results of the proposed method on higher number of plane waves are illustrated in Fig. 4. The indexes of Table 1 as well as Fig. 4 confirm that CPWC improves the image quality. As for CPWC, we do not repeat beamforming for each angle and use the apodiza-

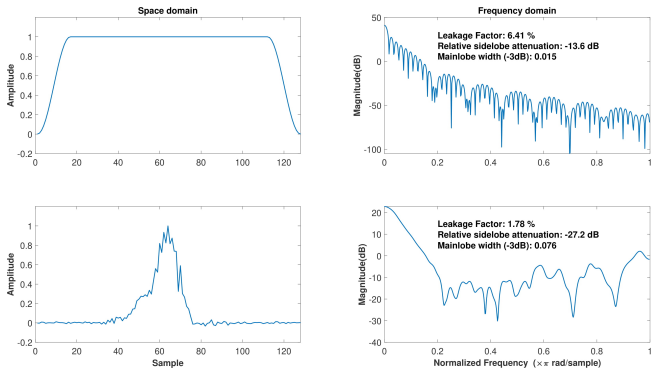

Figure 5: Comparison of apodization window estimated using ICA (second row) and Tukey25 (first row) used in DAS. Windows are shown in both space and frequency domains.

tion weights of the 0° plane wave for the remaining angles. Moreover, to limit the sources of achieved improvement, we do not apply any angular apodization. In fact, our main focus is on beamforming of the received signals.

To better understand the effect of proposed method, Fig. 5 shows a com-
310 parison between Tukey25 window used in DAS and the apodization weights estimated by ICA on ER dataset. The estimated window has a lower leakage, calculated as the ratio of power in the sidelobes to the total power, factor as well as a relative side lobe attenuation while its main lobe is wider. The

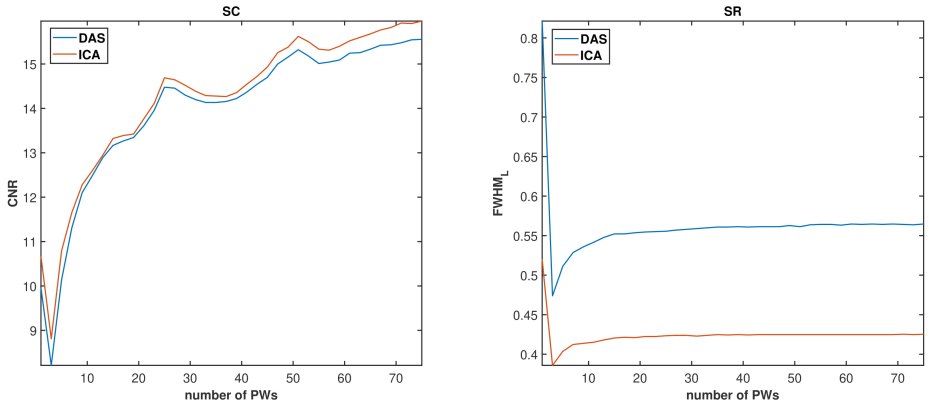

Figure 6: Quantitative comparison of beamforming results using different number of plane waves. Left column indicates SC case while right column corresponds to SR case.

Table 1: Quantitative results in terms of CNR and FWHM indexes for simulation and real phantom experiments.

dataset		SR		ER		SC	EC
index		$FWHM_A$	$FWHM_L$	$FWHM_A$	$FWHM_L$	CNR	CNR
1 PW	DAS	0.4	0.82	0.57	0.88	9.95	8.15
	ICA	0.39	0.52	0.57	0.81	10.67	8.9
11 PW	DAS	0.4	0.54	0.56	0.54	12.48	11.25
	ICA	0.4	0.41	0.56	0.51	12.6	11.4
75 PW	DAS	0.4	0.56	0.56	0.56	15.55	12
	ICA	0.4	0.42	0.56	0.53	15.96	12.1

estimated window is of a different shape which can not be found among predefined common windows. So, this point confirms the necessity of estimating the apodization window from the received data.

Fig. 6 demonstrates qualitative improvements with ICA and DAS methods as a function of the number of PWs. As can be seen in Fig. 6, the proposed approach achieves better lateral resolution with only 3 plane waves compared with DAS using 75 angles. In terms of contrast, however, the proposed approach achieves better CNR with 51 plane waves compared with DAS using 75 angles. Therefore, it is possible to reduce the number of plane wave transmits needed to achieve image quality similar to a fully sampled transmit.

3.2. In vivo Data

In real ultrasound tissues, there are more sources of degradation in image quality. In order to make sure that the proposed method also works on *in vivo* data, the results of beamforming on real carotid images of PICMUS dataset are provided in Fig. 7. Visual comparison of beamformed images with different number of angles reveals that ICA outperforms classical DAS in both cross as well as longitudinal sections. Furthermore, ICA results in sharper images with a better contrast.

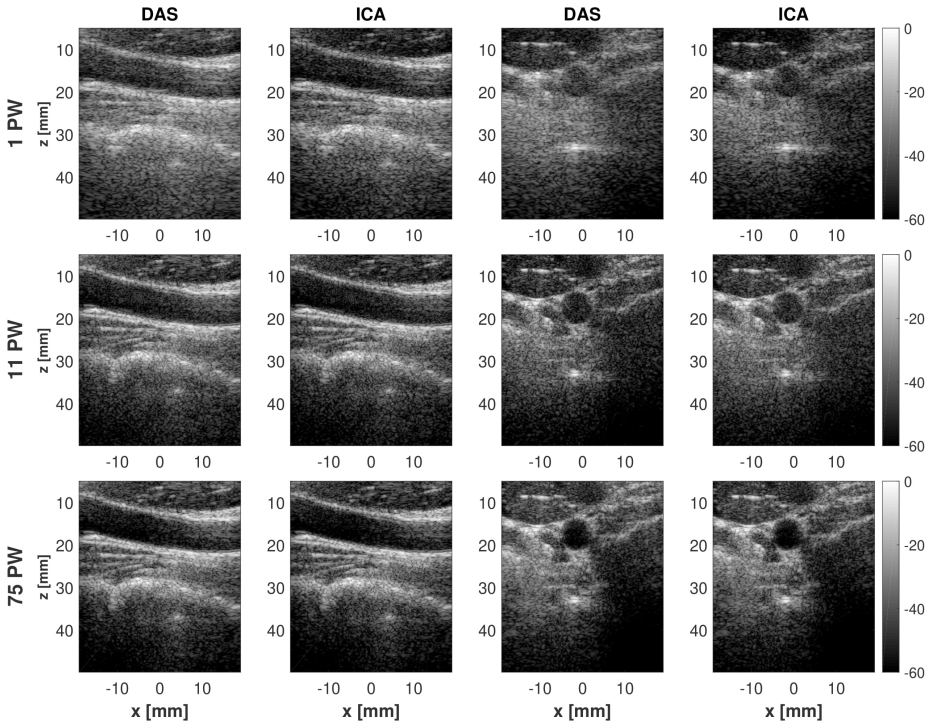

Figure 7: Beamforming results on *in vivo* data using 1, 11, and 75 plane waves. Two columns in left indicate cross-section images while left two columns correspond to longitudinal-section. Rows denote different number of transmitted plane waves used in beamforming.

3.3. Comparison with Other Adaptive Methods

As mentioned before, our focus in current study is on beamforming of the received signals. So, comparison with other adaptive approaches is of crucial importance. In this way, we present the results of five well-known approaches, namely MV [3], EMV [4], CF [8], generalized CF (GCF) [8], and PCF [9]. The comparison with these methods was not possible without using codes provided by Rindal *et al.* [39] in ultrasound toolbox repository (`http://www.ustb.no/publications/dynamic_range/`). The parameters used in the MV and EMV methods are specified next to enable interested readers to reproduce the presented results. The subarray size equals half of the number of crystal elements (64 in our case), the temporal averaging factor is given by 1.5, and the regularization factor (i.e., the diagonal loading) is 0.01. In the EMV

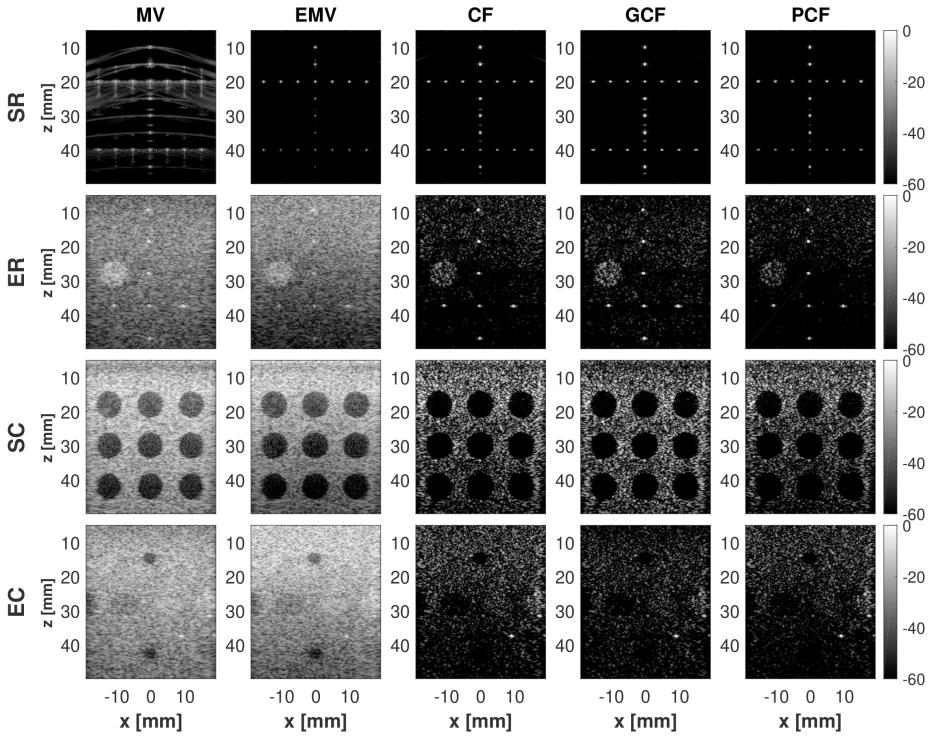

Figure 8: Results of other adaptive beamforming methods on the single 0° plane wave. Columns indicate different image data sets while rows correspond to different adaptive beamforming methods.

approach, all eigenvectors of the covariance matrix are considered in creating the signal subspace. Fig. 8 shows the result of different adaptive beamforming algorithms on a single 0° plane wave of simulated and experimental data. The quantitative comparison is provided in Table 2. The EMV method outperforms all other methods, even our proposed method, in terms of indices. However, methods based on the MV are very time consuming and are not practical for online applications. In terms of computational time, our proposed method typically takes 75 milliseconds to estimate the apodization window while MV and EMV take a few minutes, and CF methods take one second. The approaches based on CF outperform the proposed approach in terms of FWHM index while are worse in terms of contrast.

Table 2: Quantitative results of other adaptive beamforming methods in terms of CNR and FWHM indexes for simulation and real phantom experiments.

dataset		SR		ER		SC	EC
index		$FWHM_A$	$FWHM_L$	$FWHM_A$	$FWHM_L$	CNR	CNR
	MV	0.41	0.1	0.59	0.43	11.1	7.95
	EMV	0.39	0.09	0.58	0.33	12	8.1
1 PW	CF	0.32	0.44	0.48	0.47	8.2	6.3
	GCF	0.32	0.43	0.48	0.47	8.1	6.3
	PCF	0.29	0.37	0.46	0.41	6.9	5.2
	MV	0.43	0.1	0.59	0.29	11.4	9.8
	EMV	0.4	0.09	0.56	0.28	15.2	11.5
11 PW	CF	0.37	0.37	0.55	0.37	11.9	10.2
	GCF	0.38	0.36	0.55	0.37	11.8	10.2
	PCF	0.37	0.3	0.55	0.31	11	9.05
	MV	0.43	0.1	0.58	0.31	14.7	11
	EMV	0.4	0.09	0.56	0.29	17	10.4
75 PW	CF	0.4	0.38	0.56	0.38	14.05	10
	GCF	0.4	0.38	0.56	0.38	13.9	10
	PCF	0.39	0.29	0.56	0.32	14.13	10.3

4. Discussion

If we do not consider the f# in constructing the observation matrix, all pixels contribute equally in specifying the elements' weights. In practice, the backscattered signals from pixels located at shallow regions are recorded precisely by a small subset of elements close to the pixel location. The backscattered signals originating from the subordinate pixels, however, can be properly recorded by most of the elements. Therefore, it makes more sense to restrict the trace of each pixel only to its corresponding elements. Otherwise, ICA fails to estimate the source and apodization windows, leading to images that are even lower in quality than DAS.

Using a part of samples of each channel which only correspond to the middle part of the final image is important from two aspects. First, it removes the effect of incomplete data of borders on the ICA performance. Second, the FastICA algorithm converges faster as it works with a lower amount of data. Note that the estimated apodization weights and its specifications such as width of main

lobe or the amount of side lobe attenuation in each dataset are different. So, it can be concluded that there is not a unique solution that works for all data. It is worth mentioning that although the f# is applied before ICA, it does not imply that some of the probe elements are ignored completely. More specifically, as shown in Fig. 2, the entire aperture is used in constructing the observation matrix X. The trace of considered pixels, therefore, may be in some or all of r_i depending on the location of the pixel.

The algorithm can be separately applied to estimate weights associated with different insonification angles. However, the weights for different angles are not much different, overall improvement is negligible, and processing time is increased by a multiple equal to the number of angles. The angular apodization can also be estimated using ICA for CPWC. However, the main focus of this study was apodization of the received signals. To limit the sources of improvement, the angular weights are not used which also makes the comparison with other approaches possible.

As for the agreement between ICA assumptions with the nature of our problem, it is shown in [40] that the underlying statistics of ultrasound pressure field is Gaussian. However, as mentioned in Section 2.1 and shown in [35], the ICA can still be used even if only one of the independent components is Gaussian. Therefore, we can use the ICA algorithm to estimate the desired discretized map of scatterers as the only Gaussian component. In future, we plan to use IQ data using the FastICA algorithm developed for complex-valued data [41].

5. Conclusions

We have proposed a new beamforming approach for ultrasound plane-wave imaging based on ICA. Beamforming has been formalized as the estimation of one independent image out of several non-independent observation and the apodization weights have been estimated based on collected data. The images of one single plane-wave transmission as well as multiangle plane-wave acquisitions have been successfully reconstructed. Results show that the proposed method

simultaneously improves the resolution and contrast while the resulting image is also visually appealing.

6. Declaration of Competing Interest

All authors declare that the manuscript is not affected by any conflict of interests, financial and personal relationships with other people or organisations that could inappropriately influence this work.

Acknowledgements

This project was funded by NSERC Discovery grants RGPIN-2020-04612 and RGPIN-2017-06629. The authors would like to thank the organizers of the PICMUS challenge as well as the ultrasound toolbox for providing publicly available codes and data.

References

[1] M. Tanter, M. Fink, Ultrafast imaging in biomedical ultrasound, IEEE Transactions on Ultrasonics, Ferroelectrics, and Frequency Control 61 (1) (2014) 102–119. doi:10.1109/TUFFC.2014.2882.

[2] G. Montaldo, M. Tanter, J. Bercoff, N. Benech, M. Fink, Coherent plane-wave compounding for very high frame rate ultrasonography and transient elastography, IEEE Transactions on Ultrasonics, Ferroelectrics, and Frequency Control 56 (3) (2009) 489–506. doi:10.1109/TUFFC.2009.1067.

[3] J. Synnevag, A. Austeng, S. Holm, Benefits of minimum-variance beamforming in medical ultrasound imaging, IEEE Transactions on Ultrasonics, Ferroelectrics, and Frequency Control 56 (9) (2009) 1868–1879. doi:10.1109/TUFFC.2009.1263.

[4] B. M. Asl, A. Mahloojifar, Eigenspace-based minimum variance beamforming applied to medical ultrasound imaging, IEEE Transactions on Ultrasonics, Ferroelectrics, and Frequency Control 57 (11) (2010) 2381–2390. doi:10.1109/TUFFC.2010.1706.

[5] J. F. Synnevag, A. Austeng, S. Holm, Adaptive beamforming applied to medical ultrasound imaging, IEEE Transactions on Ultrasonics, Ferroelectrics, and Frequency Control 54 (8) (2007) 1606–1613. doi:10.1109/TUFFC.2007.431.

[6] A. C. Jensen, A. Austeng, An approach to multibeam covariance matrices for adaptive beamforming in ultrasonography, IEEE Transactions on Ultrasonics, Ferroelectrics, and Frequency Control 59 (6) (2012) 1139–1148. doi:10.1109/TUFFC.2012.2304.

[7] R. Mallart, M. Fink, Adaptive focusing in scattering media through sound-speed inhomogeneities: The van cittert zernike approach and focusing criterion, The Journal of the Acoustical Society of America 96 (6) (1994) 3721–3732. doi:10.1121/1.410562.

[8] Pai-Chi Li, Meng-Lin Li, Adaptive imaging using the generalized coherence factor, IEEE Transactions on Ultrasonics, Ferroelectrics, and Frequency Control 50 (2) (2003) 128–141. doi:10.1109/TUFFC.2003.1182117.

[9] J. Camacho, M. Parrilla, C. Fritsch, Phase coherence imaging, IEEE Transactions on Ultrasonics, Ferroelectrics, and Frequency Control 56 (5) (2009) 958–974. doi:10.1109/TUFFC.2009.1128.

[10] N. Q. Nguyen, R. W. Prager, Minimum variance beamformers for coherent plane-wave compounding, in: N. Duric, B. Heyde (Eds.), Medical Imaging 2017: Ultrasonic Imaging and Tomography, Vol. 10139, International Society for Optics and Photonics, SPIE, 2017, pp. 254 – 263. doi:10.1117/12.2254293.

[11] O. M. H. Rindal, A. Austeng, Double adaptive plane-wave imaging, in: 2016 IEEE International Ultrasonics Symposium (IUS), 2016, pp. 1–4. doi:10.1109/ULTSYM.2016.7728906.

[12] A. M. Deylami, J. A. Jensen, B. M. Asl, An improved minimum variance beamforming applied to plane-wave imaging in medical ultrasound, in: 2016 IEEE International Ultrasonics Symposium (IUS), 2016, pp. 1–4. doi:10.1109/ULTSYM.2016.7728895.

[13] F. Varray, M. Azizian Kalkhoran, D. Vray, Adaptive minimum variance coupled with sign and phase coherence factors in iq domain for plane wave beamforming, in: 2016 IEEE International Ultrasonics Symposium (IUS), 2016, pp. 1–4. doi:10.1109/ULTSYM.2016.7728903.

[14] N. Q. Nguyen, R. W. Prager, A spatial coherence approach to minimum variance beamforming for plane-wave compounding, IEEE Transactions on Ultrasonics, Ferroelectrics, and Frequency Control 65 (4) (2018) 522–534. doi:10.1109/TUFFC.2018.2793580.

[15] Congzhi Wang, Xi Peng, Dong Liang, Hairong Zheng, Plane-wave ultrasound imaging based on compressive sensing with low memory occupation, in: 2015 IEEE International Ultrasonics Symposium (IUS), 2015, pp. 1–4. doi:10.1109/ULTSYM.2015.0309.

[16] G. David, J.-l. Robert, B. Zhang, A. F. Laine, Time domain compressive beam forming of ultrasound signals, The Journal of the Acoustical Society of America 137 (5) (2015) 2773–2784.

[17] A. Besson, M. Zhang, F. Varray, H. Liebgott, D. Friboulet, Y. Wiaux, J. Thiran, R. E. Carrillo, O. Bernard, A sparse reconstruction framework for fourier-based plane-wave imaging, IEEE Transactions on Ultrasonics, Ferroelectrics, and Frequency Control 63 (12) (2016) 2092–2106.

[18] A. Besson, D. Perdios, F. Martinez, Z. Chen, R. E. Carrillo, M. Arditi, Y. Wiaux, J. Thiran, Ultrafast ultrasound imaging as an inverse problem:

Matrix-free sparse image reconstruction, IEEE Transactions on Ultrasonics, Ferroelectrics, and Frequency Control 65 (3) (2018) 339–355.

[19] K. Dei, J. Tierney, B. Byram, Aperture domain model image reconstruction (ADMIRE) with plane wave synthesis, in: N. Duric, B. Heyde (Eds.), Medical Imaging 2017: Ultrasonic Imaging and Tomography, Vol. 10139, International Society for Optics and Photonics, SPIE, 2017, pp. 244 – 253. doi:10.1117/12.2255526.
URL https://doi.org/10.1117/12.2255526

[20] K. Dei, J. E. Tierney, B. C. Byram, Model-based beamforming with plane wave synthesis in medical ultrasound, Journal of Medical Imaging 5 (2) (2018) 1 – 12. doi:10.1117/1.JMI.5.2.027001.

[21] Jian-Yu Lu, 2d and 3d high frame rate imaging with limited diffraction beams, IEEE Transactions on Ultrasonics, Ferroelectrics, and Frequency Control 44 (4) (1997) 839–856. doi:10.1109/58.655200.

[22] D. Garcia, L. L. Tarnec, S. Muth, E. Montagnon, J. Porée, G. Cloutier, Stolt's f-k migration for plane wave ultrasound imaging, IEEE Transactions on Ultrasonics, Ferroelectrics, and Frequency Control 60 (9) (2013) 1853–1867. doi:10.1109/TUFFC.2013.2771.

[23] O. Bernard, M. Zhang, F. Varray, P. Gueth, J. Thiran, H. Liebgott, D. Friboulet, Ultrasound fourier slice imaging: a novel approach for ultrafast imaging technique, in: 2014 IEEE International Ultrasonics Symposium, 2014, pp. 129–132. doi:10.1109/ULTSYM.2014.0033.

[24] T. Szasz, A. Basarab, D. Kouamé, Beamforming through regularized inverse problems in ultrasound medical imaging, IEEE Transactions on Ultrasonics, Ferroelectrics, and Frequency Control 63 (12) (2016) 2031–2044. doi:10.1109/TUFFC.2016.2608939.

[25] E. Ozkan, V. Vishnevsky, O. Goksel, Inverse problem of ultrasound beamforming with sparsity constraints and regularization, IEEE Transactions on

Ultrasonics, Ferroelectrics, and Frequency Control 65 (3) (2018) 356–365. doi:10.1109/TUFFC.2017.2757880.

[26] T. Chernyakova, D. Cohen, M. Shoham, Y. C. Eldar, imap beamforming for high-quality high frame rate imaging, IEEE Transactions on Ultrasonics, Ferroelectrics, and Frequency Control 66 (12) (2019) 1830–1844.

[27] R. R. Wildeboer, F. Sammali, R. J. G. Van Sloun, Y. Huang, P. Chen, M. Bruce, C. Rabotti, S. Shulepov, G. Salomon, B. C. Schoot, H. Wijkstra, M. Mischi, Blind source separation for clutter and noise suppression in ultrasound imaging: Review for different applications, IEEE Transactions on Ultrasonics, Ferroelectrics, and Frequency Control (2020) 1–1.

[28] A. C. H. Yu, L. Lovstakken, Eigen-based clutter filter design for ultrasound color flow imaging: a review, IEEE Transactions on Ultrasonics, Ferroelectrics, and Frequency Control 57 (5) (2010) 1096–1111.

[29] J. E. Tierney, D. M. Wilkes, B. C. Byram, Independent component analysis-based tissue clutter filtering for plane wave perfusion ultrasound imaging, in: Medical Imaging 2019: Ultrasonic Imaging and Tomography, Vol. 10955, International Society for Optics and Photonics, 2019, p. 1095503.

[30] C. M. Gallippi, K. R. Nightingale, G. E. Trahey, Bss-based filtering of physiological and arfi-induced tissue and blood motion, Ultrasound in medicine & biology 29 (11) (2003) 1583–1592.

[31] P. Li, X. Yang, D. Zhang, Z. Bian, Adaptive clutter filtering based on sparse component analysis in ultrasound color flow imaging, IEEE Transactions on Ultrasonics, Ferroelectrics, and Frequency Control 55 (7) (2008) 1582–1596.

[32] C. M. Gallippi, G. E. Trahey, Adaptive clutter filtering via blind source separation for two-dimensional ultrasonic blood velocity measurement, Ultrasonic imaging 24 (4) (2002) 193–214.

[33] K. Dei, S. Schlunk, B. Byram, Computationally efficient implementation of aperture domain model image reconstruction, IEEE Transactions on Ultrasonics, Ferroelectrics, and Frequency Control 66 (10) (2019) 1546–1559.

[34] H. Liebgott, A. Rodriguez-Molares, F. Cervenansky, J. A. Jensen, O. Bernard, Plane-wave imaging challenge in medical ultrasound, in: 2016 IEEE International Ultrasonics Symposium (IUS), 2016, pp. 1–4. doi:10.1109/ULTSYM.2016.7728908.

[35] A. Hyvärinen, E. Oja, Independent component analysis: algorithms and applications, Neural Networks 13 (4) (2000) 411 – 430. doi:https://doi.org/10.1016/S0893-6080(00)00026-5.
URL http://www.sciencedirect.com/science/article/pii/S0893608000000265

[36] A. Hyvärinen, New approximations of differential entropy for independent component analysis and projection pursuit, in: Advances in neural information processing systems, 1998, pp. 273–279.

[37] A. Hyvarinen, Fast and robust fixed-point algorithms for independent component analysis, IEEE Transactions on Neural Networks 10 (3) (1999) 626–634. doi:10.1109/72.761722.

[38] J. H. Friedman, J. W. Tukey, A projection pursuit algorithm for exploratory data analysis, IEEE Transactions on Computers C-23 (9) (1974) 881–890. doi:10.1109/T-C.1974.224051.

[39] O. M. H. Rindal, A. Austeng, A. Fatemi, A. Rodriguez-Molares, The effect of dynamic range alterations in the estimation of contrast, IEEE Transactions on Ultrasonics, Ferroelectrics, and Frequency Control 66 (7) (2019) 1198–1208. doi:10.1109/TUFFC.2019.2911267.

[40] R. F. Wagner, Statistics of speckle in ultrasound b-scans, IEEE Trans. Sonics & Ultrason. 30 (3) (1983) 156–163.

[41] E. Bingham, A. Hyvärinen, A fast fixed-point algorithm for independent component analysis of complex valued signals, International journal of neural systems 10 (01) (2000) 1–8.